Three-Dimensional Structure of P3HT Assemblies in Organic Solvents Revealed by Cryo-TEM

ARTICLE *in* NANO LETTERS · FEBRUARY 2014

Impact Factor: 13.59 · DOI: 10.1021/nl5001967 · Source: PubMed

NANO LETTERS

Letter

pubs.acs.org/NanoLett

Three-Dimensional Structure of P3HT Assemblies in Organic Solvents Revealed by Cryo-TEM

Maarten J. M. Wirix,[†,‡] Paul H. H. Bomans,[†] Heiner Friedrich,[†] Nico A. J. M. Sommerdijk,[†] and Gijsbertus de With*,[†]

[†]Laboratory for Materials and Interface Chemistry and Soft Matter Cryo-TEM Research Unit, Eindhoven University of Technology, P.O. Box 513, Eindhoven, 5600 MB, The Netherlands

[‡]Dutch Polymer Institute (DPI), P.O. Box 902, 5600 AX Eindhoven, The Netherlands

Supporting Information

ABSTRACT: Poly(3-hexylthiophene) (P3HT) assemblies in vitrified organic solvents were visualized at nanometer scale resolution by cryo-transmission electron microscopy, low dose electron diffraction, and cryo-tomography revealing a three-dimensional lamellar structure formed by the stacking of the conjugated backbones of P3HT with a distance of 1.7 nm and increased order in the bulk of the nanowire. This combination of techniques reveals local structures in dispersion and the condensed state that play a crucial role in the performance of organic electronic devices.

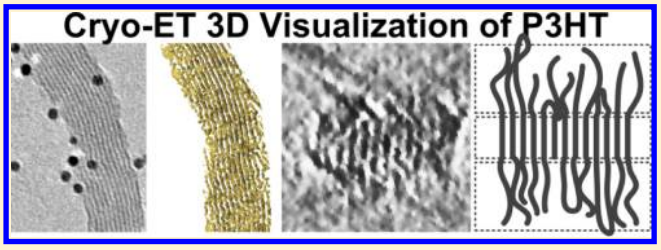

KEYWORDS: *P3HT, polymer crystal, cryo, electron microscopy, nanowire, organic solvent*

During the past decade poly(3-hexylthiophene) P3HT has become one of the most used components in organic electronics.[1,2] P3HT is a conjugated polymer, which has a tendency to aggregate via the $\pi-\pi$ stacking of the conjugated backbone.[3−11] This is often beneficial for the performance of electronic devices, because the ordering is known to increase the hole mobility and results in a more phase separated materials morphology, which can lead to better performing devices.[12−15] Although in the field of organic photovoltaics there are nowadays many high-performance polymers available with some even surpassing the 10% power conversion efficiency, P3HT as a component in the P3HT/PCBM solar cells remains a cost-effective choice in large-scale production.[16]

Such cost-effective manufacturing of bulk-heterojunction solar cells relies on printing technology. In this case, the device performance depends on a long list of processing conditions, one of them being the ink used, possibly containing preformed nanostructures. Therefore reliable ways to characterize these inks, which are usually based on (halogenated) organic solvents, are needed. In many cases, compromises like drying, diluting, changing solvent, and so forth are needed to make these inks compatible with characterization techniques like UV−vis, atomic force microscopy, transmission electron microscopy (TEM), wide-angle X-ray diffraction, small-angle X-ray spectroscopy, small-angle neutron scattering, and NMR. In addition, the result of the analysis often is also dependent on the model that was used to interpret the data. On the other hand, cryo-TEM, capable of in situ characterizing organic solutions, is a good alternative that does not need these compromises and enables characterization of the solution structures in their equilibrium state.[17] In the last few decades, cryo-TEM sample preparation techniques have evolved from pioneering setups for plunge freezing of aqueous samples[18,19] to advanced vitrification robots (vitrobots) with atmospheric and temperature control that can quickly and reliably vitrify films of (organic) solvents.[20−24]

In the present study, we utilize cryo-TEM as a means to characterize P3HT assemblies in solution. The assemblies were made by first dissolving P3HT at higher temperature and subsequently cooling the solutions to induce the thermochromic phase transition.[25,26] We used both toluene, a non-halogated solvent, and 1,2-dichlorobenzene (oDCB), a halogenated solvent, to illustrate the potential of cryo-TEM for the general purpose of characterizing photovoltaic inks.

A P3HT concentration of 1 wt %, representative for solution processing of organic electronic devices, was used. Conventionally, developing aggregation in solution is assessed by UV−vis. For obtaining UV−vis spectra, the solutions/dispersions have to be diluted by, for example, 1:10, and recorded using a thin cuvette because P3HT has such a high optical density that transmission for a nondiluted sample will be very small. In the UV−vis absorption spectra of diluted solutions, Figure 1c, the formation of aggregates can be seen as a red shift in the absorption spectrum when comparing the isotropic solutions with the dispersions. This red shift is usually attributed to an increase in $\pi-\pi$ stacking of the polymer chains.[27] In the HJ-aggregate model,[28] this increased $\pi-\pi$ stacking corresponds to

Received: January 17, 2014
Revised: February 26, 2014
Published: February 28, 2014

dx.doi.org/10.1021/nl5001967 | *Nano Lett.* 2014, 14, 2033−2038

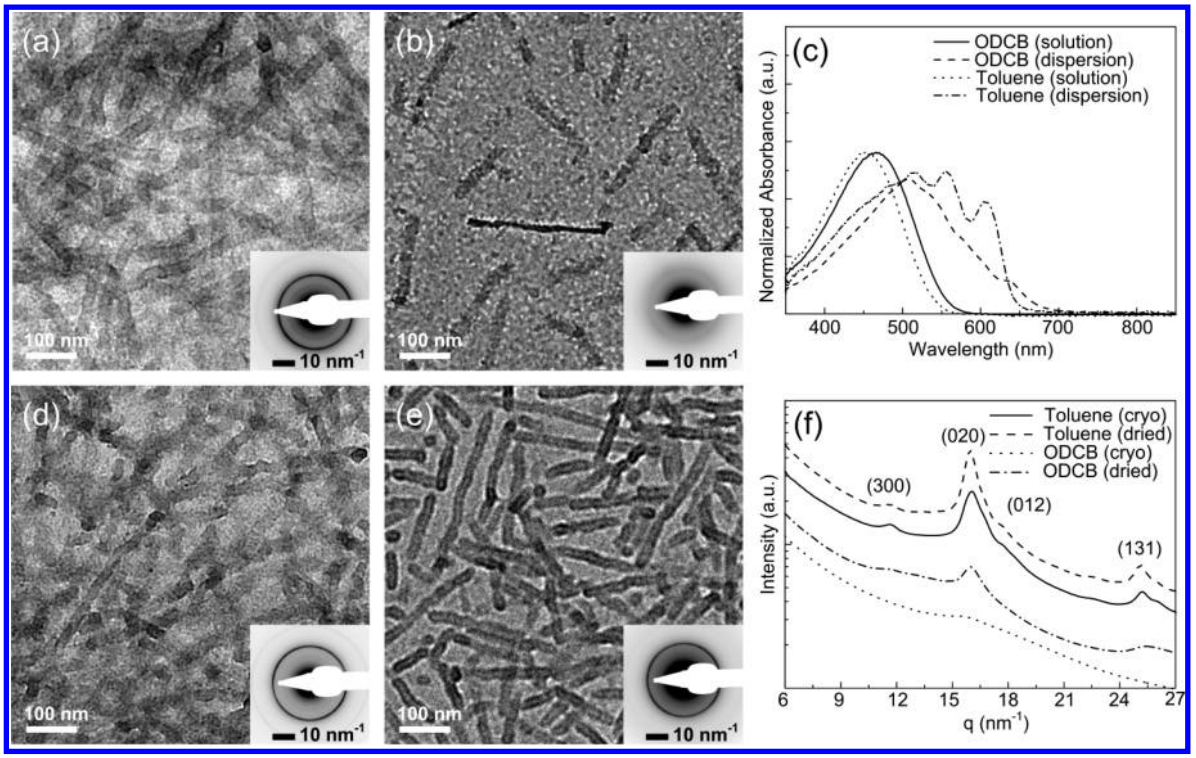

Figure 1. Cryo-TEM images of vitrified solutions of P3HT 1 wt %, aged for > 7 days (a) in toluene and (b) in oDCB. (c) UV−vis absorption spectra of the initial solution and aged dispersion. Same solutions dropcast and blotted on a carbon support film of a TEM grid in (d) toluene and (e) oDCB; insets are the (cryo-)LDED patterns corresponding to the samples. (f) Radially integrated (cryo-)LDED patterns.

an increase in interchain coupling (J_{inter}) as compared to the isolated chains ($J_{inter} = 0$). This parameter can be estimated by taking the ratio between the lowest energy peak (A_{0-0}) and the next replica peak (A_{0-1}) heights.[29] Because it was shown that this ratio for isolated P3HT chains is ∼1,[30] the clearly lower-than-one ratios for both the toluene and oDCB dispersions indicate interaction between the P3HT chains, which makes them H-type aggregates. The maximum for absorption for the P3HT solution in oDCB is located at slightly higher wavelength than the maximum for the toluene solution, because oDCB better solvates the conjugated backbone of the thiophene, thus resulting in more extended chains and longer conjugation lengths in the solution. In the HJ-aggregate model, this corresponds to a higher intrachain interaction (J_{intra}) as compared to the chains in toluene. Both the dispersions in oDCB and in toluene show the similar red shift. However, for the toluene samples the vibronic fine structure is very pronounced, while the oDCB samples show more peak broadening, because of the stronger polymer−solvent interaction. Note that this provides global information on a diluted state while it is desirable to acquire structural information on a local scale from nondiluted solutions and dispersions, as used for processing of actual devices.

Characteristics of the aggregates in actual 1 wt % dispersions were obtained with a combination of cryo-TEM, low-dose electron diffraction (LDED), and cryo-tomography, the latter technique revealing the three-dimensional (3D) nanostructure of the P3HT assemblies in detail. The structure of P3HT, necessary to explain the properties of functional devices, has been deduced using a wide range of characterization techniques,[25,26,31−33] but has never been visualized in 3D, which can conveniently be done in solution, that is, the native state.

These dispersions were subsequently vitrified and visualized with cryo-TEM (Figure 1a,b). In the toluene dispersion, we observe many nanowires with a width of 20−30 nm, and >100 nm in length. Detailed size analysis of the images is added in Figure S1 in the Supporting Information. The inset (cryo-)LDED pattern shows a clearly visible ring (powder pattern) at d = 0.38 nm (q = 16.5 nm^{-1}) that corresponds to the $\pi-\pi$ stacking of the thiophene chains. Because the limited thickness of the solvent layer, the nanowires embedded in the vitrified organic solution are confined and mostly oriented perpendicular to the electron beam. Consequently the $\pi-\pi$ stacks are oriented perpendicular too, explaining the strong contribution of this reflection. In the oDCB dispersion similar nanowires were found, but they were much less abundant because oDCB is a good solvent for P3HT and is less likely to promote nanowire formation given the applied conditions. The inset (cryo-)LDED pattern only shows a very diffuse diffraction ring at d = 0.38 nm, indicating less ordering in the solution. The dried samples of the toluene and oDCB dispersions, depicted respectively in Figure 1d,e, show a rather similar dense packing of P3HT nanowires. The toluene solution was saturated with P3HT crystals and no significant change in the amount of aggregates due to drying can be seen. The dried oDCB dispersion samples on the other hand contain more wires that indicates that a substantial amount of them has been formed during drying. When comparing the cryo-samples of the nonaggregated P3HT dissolved in oDCB with the dried equivalents, this effect is even more pronounced. No aggregation in solution was observed using cryo-TEM while the dried sample contains many crystals (Supporting Information Figure S1). Size analysis (Supporting Information Figure S2) revealed no significant difference in wire dimensions in the cryo and dried samples of toluene and oDCB. On the

dx.doi.org/10.1021/nl5001967 | Nano Lett. 2014, 14, 2033−2038

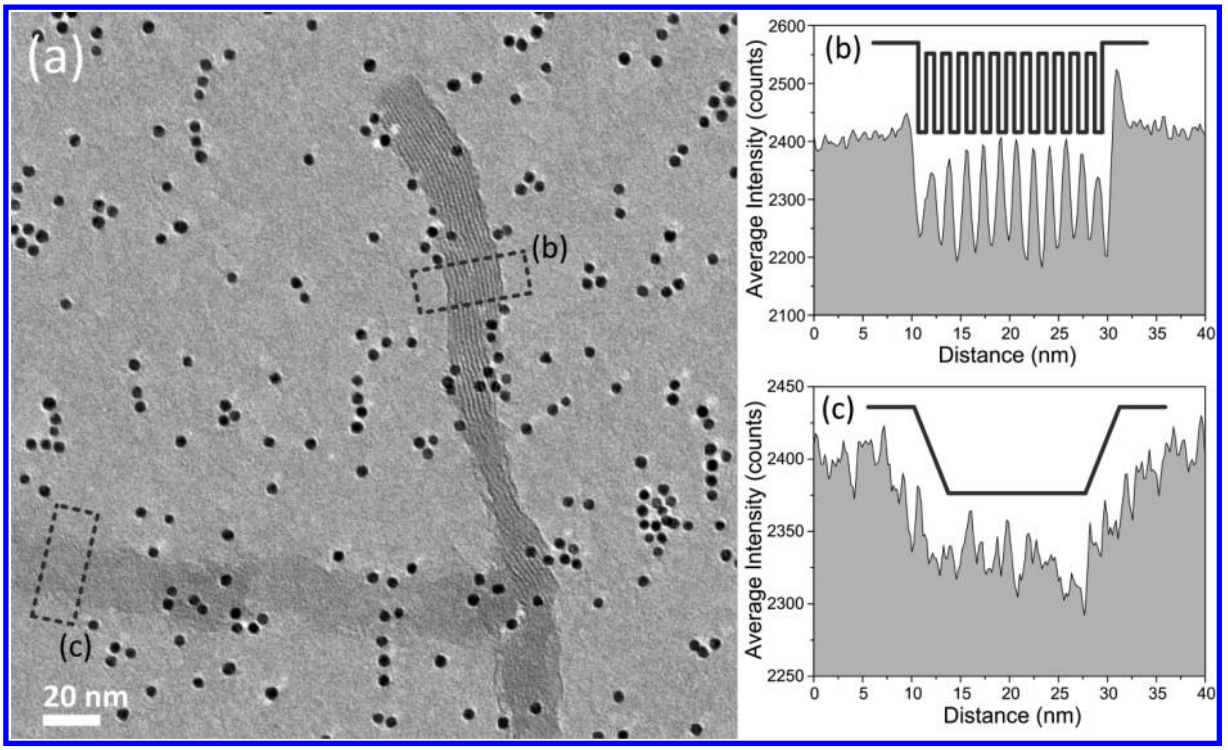

Figure 2. (a) Cryo-TEM image of two P3HT nanowires with different orientations, vitrified in oDCB. Three to five nanometer thiol surface-modified Au markers are present for the purpose of electron tomography. The averaged line profile from box (b) showing sharp interfaces and the 1.7 nm lamellar stacking while the profile for box (c) shows diffuse interfaces.

basis of this analysis, we conclude that in toluene and oDCB dispersions the same nanowires are formed.

The oDCB dispersion contains less ordered aggregates resulting in a lower diffraction strength of the $\pi-\pi$ stacking band in the LDED pattern, as compared to the toluene dispersion. In Figure 1f, all the diffraction patterns are radially integrated and their intensities given as function of q. The dried samples have a higher and sharper diffraction peak at q = 16.5 nm^{-1}, because drying promotes crystallization. The diffraction peak intensity of the oDCB dispersions, both for the cryo and the dried samples, is lower as compared to the toluene dispersions, which shows that under similar conditions oDCB is less likely to promote the formation of ordered crystalline nanowires than toluene. This is completely in line with the fact that oDCB is a good solvent for P3HT, while toluene is a relatively poor solvent for P3HT. In addition, three weaker reflections were observed for the toluene sample only at d = 0.54 nm (q = 11.6 nm^{-1}), d = 0.35 nm (q = 17.8 nm^{-1}), and d = 0.25 nm (q = 24.8 nm^{-1}) corresponding to the (300), (012), and (131) planes, respectively.[32] This in consonance with the UV−vis spectra is another indication that toluene promotes nanowire formation to a much greater extent than oDCB.

Roehling et al. conclude in their study from UV−vis and powder XRD data that a higher degree of intra- and interchain order is obtained in nanofibers formed from better solvents. However, their UV−vis spectrum for P3HT aggregates in anisole looks very similar as our UV−vis spectrum of the P3HT dispersion in toluene. In our case, the higher ordered aggregates in toluene were achieved by slowing down the crystallization rate by crystallizing at higher temperature. In comparison with anisole, oDCB is such a good solvent that the equilibrium between aggregated and solvated molecules is shifted largely toward solvated molecules. Hence taking into account the difference in crystallization rate, these combined results provide a clear picture of the possibility to achieve ordered P3HT aggregates by exploiting solubility differences, solvent quality, and crystallization kinetics, as was clearly identified in the work by Roehling et al.[29]

Summarizing so far, both dried samples show that many nanowires are formed, but in the case of the toluene sample most of the nanowires were already present in solution. However, there is a significant increase in the amount of aggregates upon drying the oDCB dispersion and the aggregates exhibit overall less crystalline ordering as compared to the toluene samples. Cryo-TEM is an indispensable technique to characterize in situ the structures in solution and dispersions, providing a representative view of the nature and the amount of structures.

Apart from observing mesoscopic features such as wire length, orientation, and diameter distribution, or overall crystallinity, we also performed high-resolution imaging to investigate the local 3D morphology of the P3HT nanowires in solution. For this purpose, 3−5 nm Au fiducial markers were added to the oDCB dispersion to aid in the alignment of the electron tomography data set. In Figure 2a, one image of the tilt-series is displayed showing two intersecting P3HT nanowires and many 3−5 nm Au markers. The vertical wire is oriented with the polymer chains extended parallel to the electron beam (top view), while the horizontal wire is oriented with the polymer chains perpendicular to the electron beam (side view). For the vertical wire, the lamellar stacking can be clearly seen along its length. Plotting a line profile across the lamellar stacks, as shown in Figure 2b, shows a periodically varying contrast. Because lamellae, formed by the $\pi-\pi$ stacking of the conjugated backbones, have a much higher mass density and mean inner potential than the stacks of aliphatic side chains

dx.doi.org/10.1021/nl5001967 | Nano Lett. 2014, 14, 2033−2038

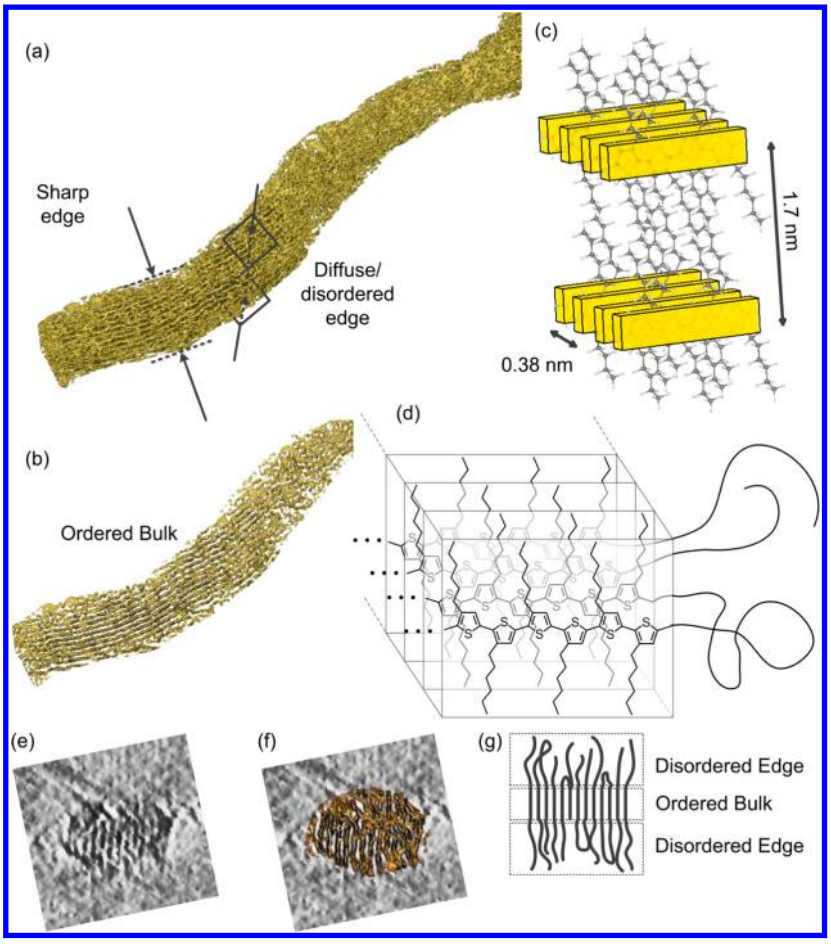

Figure 3. (a) Isosurface generated from tomographic reconstruction of a P3HT nanowire. (b) Isosurface from the middle of the nanowire showing increased order. (c) Model of the lamellar order in the middle of the nanowire. (d) Model showing crystalline order in the bulk and disorder on the side of the nanowire. (e) Slice from the tomographic reconstruction showing a cross-section of the wire. (f) The same slice overlaid with the corresponding segment of the segmented structure. (g) Cartoon depicting the ordered bulk and the disordered edges.

between them, the former will show up as dark fringes in the cryo-TEM image. Analyzing the periodicity, there are 12 lamellae bridging a distance of ∼ 20 nm. This corresponds nicely to the 1.7 nm stacking distance between the lamellae, corresponding to the (100) reflection in X-ray scattering experiments[34] and as also sometimes observed in LDED.[11] Here it has been observed for the first time in cryo-conditions. In comparison with the previously reported P3HT wires made by the whisker method[4] with high aspect ratio (width versus thickness), these nanowires have a more comparable width and thickness. Because of the shape anisotropy of the wires (width versus thickness) in dried samples or spin-coated films, these lamellar stacks are usually perpendicular to the electron beam and therefore not observable by TEM. Alternatively, due to the preferential orientation of these wires, their presence can be verified with grazing incidence X-ray diffraction (GIXRD).[35] In Figure 2c, an average intensity profile of the wire with lamellae perpendicular to the electron beam direction is shown. The contrast is much lower here and the high electron density regions are now oriented parallel to the electron beam. Consequently, the path length through the strong scattering region is shorter because of the orientation and the thickness. Additionally, this average intensity profile reveals diffuse edges in sharp contrast with intensity profile of the vertical wire (Figure 2b) with well-defined edges and periodicity. Schematic intensity profiles illustrating this point are shown as insets.

Finally, a tomography series was acquired for the vertically oriented nanowire. The fact that the nanowires are embedded in a vitrified film makes them more beam stable and also increases the structural integrity as compared to a wire that is suspended over a hole of lacy carbon or a quantifoil TEM grid. In addition, the cryogenic film gives rise to more contrast than a support film which is often made up from 10 to 30 nm carbon and reduces contrast significantly for organic polymers. A thinner carbon support could be used but this would complicate sample preparation due to the weaker support film and does not solve the preferential orientation of the nanowire on a carbon support. All factors taken together rendered it possible to acquire a cryo-electron tomographic series of this nanowire with unprecedented resolution. The dose rate was calibrated to 2500 e^{-} nm^{-2} s^{-1} with a total accumulated dose of ∼ 2 × 10^{5} e^{-} nm^{-2}. This tomographic series was subsequently reconstructed using a weighted back projection method. The results are summarized in Figure 3. For an animation of the 3D structure of the nanowire as well as further details about acquisition, reconstruction, and segmentation, see the Supporting Information.

In Figure 3a, a cryo-ET derived segmentation of the lamellar stacks is shown. Segmentation of the reconstruction of the nanowire was done by calculating a cross-correlation between the 3D volume and a sphere that has a size comparable to the estimated size of the lamella, as observed from the slices, in

dx.doi.org/10.1021/nl5001967 | *Nano Lett.* 2014, 14, 2033−2038

every point of the volume. In this way, we get a 3D correlation map that preferentially filters out the lamella. Next, the lamella were segmented out by using a top hat threshold. A mask was generated that enveloped the wire and then was used to cut out the surrounding material. Subsequently a binary segmentation of the lamella in the nanowire was acquired. The regions that are colored, corresponding to the low intensity regions in the tomographic reconstruction, scatter the strongest and represent the lamellae. The background as well as the aliphatic regions are transparent. Analysis of a smaller volume from the middle of the nanowire (Figure 3b) shows a more pronounced order, that is, a clear periodicity in lamellar stacking. The bulk of the nanowire is made up from $\pi-\pi$ stacked regions that form the lamellae alternating with aliphatic regions, corresponding with the fringes in Figure 2a. A combination of our findings with the crystal structure of phase I P3HT is depicted in Figure 3c[32] in which the conjugated polymer backbones are highlighted in yellow. We refer to the direction parallel to the polymer chain as the sides of the nanowire and to the direction perpendicular to the lamellar stacks as the top and bottom. While Figure 2 shows a sharp edge for the top and bottom of the nanowire and diffuse edges for the sides of the nanowire, the tomographic model shows in addition more order in the bulk than toward the sides of the nanowire, which is in consonance with the diffuse edges. The top and bottom of the nanowire are bordered by lamellae giving rise to this sharper edge, while on the sides the polymer chains are branching out and possibly folding back giving rise to a more diffuse edge, as illustrated by the molecular model shown in Figure 3d. We can consider the morphology of this P3HT nanowire in solution as a highly ordered stack of lamellae that slowly branches out toward the sides, giving rise to more disorder. To provide an impression of the quality of the raw reconstruction, a slice of a cross-section of the reconstruction is shown in Figure 3e, which is overlaid with the corresponding segment of the segmented structure in Figure 3f. Because we do not have enough resolution to visualize individual polymer chains, it is impossible to segment the disordered parts clearly. However, we conclude from the increasing disorder toward the outer parts of the cross-section that the wires are more ordered in the bulk and more disordered at the edges, as illustrated in the cartoon in Figure 3g.

Though the structure of P3HT has been shown before in dry conditions or in functional devices,[5,6,29,31,36,37] a clear visualization of a P3HT nanowire embedded in a vitrified layer or organic solvent in cryo-TEM has, to the best of our knowledge, never been shown before. Structural information in solutions/dispersions is uncommon, but vital to understand structure formation during all the processing steps necessary for realizing an organic electronic device. Because for dispersions in halogenated solvents it is difficult to get structural information by XRD, as the halogen atoms are much stronger scatterers than the carbon based polymers under investigation, cryo-TEM provides an elegant solution. This 3D analysis visualizes the in situ structure of the wires on a nanometer scale. It is at this scale that important physical processes take place and from which characteristic behavior of P3HT like anisotropy in conductivity and electronic landscape can be inferred.

In summary, we present cryo-TEM as a technique for in situ characterizing photovoltaic inks. Typical advantages are (a) the absence of orientation bias and structural changes (unlike conventional TEM employing dried samples in which orientation and structural changes are likely induced), (b) the possibility of analyzing overlapping structures independent of optical density (unlike UV−vis), (c) the possibility to do time-resolved characterization,[38,39] and (d) the ability local information on order and disorder (unlike X-ray diffraction and UV−vis). More specifically, we investigated P3HT assemblies by embedding them in a film of a vitrified organic solvent, namely toluene and oDCB. Using these vitrified samples cryo-TEM reveals that crystallization of the oDCB dispersions largely occurs during drying. Furthermore, the stabilizing effect of the cryogenic layer allows high-resolution cryo-tomography resulting in 3D visualization showing the nanowires in different orientations. This clearly revealed the 1.7 nm spaced lamellae composed of $\pi-\pi$ stacked conjugated backbones of the P3HT along the length of the nanowire, diffuse edges in one direction and sharp edges on the other, originating from different degrees of ordering within the P3HT crystals. Insight in the anisotropy of the P3HT wires resulting from their crystal structure is important to understand the function of P3HT assemblies in organic electronic devices in terms of charge percolation, conductivity, electronic landscape, and morphology. The characterization of organic solutions/dispersions employing concentrations and solvents that are also used for the creation of such devices, therefore yields important structural information on the precursor assemblies.

■ ASSOCIATED CONTENT

Ⓢ Supporting Information

Additional cryo-TEM images and nanowire size analysis, experimental details, supporting TEM images, and an animation of the 3D structure of the P3HT nanowire. This material is available free of charge via the Internet at http://pubs.acs.org.

■ AUTHOR INFORMATION

Corresponding Author

*E-mail: G.deWith@tue.nl.

Notes

The authors declare no competing financial interest.

■ ACKNOWLEDGMENTS

Max Spapens' help with the 3D analysis is appreciated. This work forms part of the research program of the Dutch Polymer Institute (DPI), Project No. 682. Structure Creation in Solution. (Supporting Information is available online from Wiley InterScience or from the author.)

■ REFERENCES

(1) Dang, M. T.; Hirsch, L.; Wantz, G. *Adv. Mater.* **2011**, *23*, 3597−3602.
(2) Sirringhaus, H.; Brown, P. J.; Friend, R. H.; Nielsen, M. M.; Bechgaard, K.; Langeveld-Voss, B. M. W.; Spiering, A. J. H.; Janssen, R. A. J.; Meijer, E. W.; Herwig, P.; de Leeuw, D. M. *Nature* **1999**, *401*, 685−688.
(3) Liu, J.; Arif, M.; Zou, J.; Khondaker, S. I.; Zhai, L. *Macromolecules* **2009**, *42*, 9390−9393.
(4) Samitsu, S.; Shimomura, T.; Heike, S.; Hashizume, T.; Ito, K. *Macromolecules* **2008**, *41*, 8000−8010.
(5) Rodd, C. M.; Agarwal, R. *Nano Lett.* **2011**, *11*, 3460−3467.
(6) Rodd, C. M.; Agarwal, R. *Nano Lett.* **2013**, *13*, 3760−3765.
(7) Crossland, E. J.; Tremel, K.; Fischer, F.; Rahimi, K.; Reiter, G.; Steiner, U.; Ludwigs, S. *Adv. Mater.* **2012**, *24*, 839−844.
(8) Brinkmann, M. *J. Polym. Sci., Part B: Polym. Phys.* **2011**, *49*, 1218−1233.

(9) Niles, E. T.; Roehling, J. D.; Yamagata, H.; Wise, A. J.; Spano, F. C.; Moule, A. J.; Grey, J. K. *J. Phys. Chem. Lett.* **2012**, *3*, 259−263.
(10) Chou, K. W.; Yan, B.; Li, R.; Li, E. Q.; Zhao, K.; Anjum, D. H.; Alvarez, S.; Gassaway, R.; Biocca, A.; Thoroddsen, S. T.; Hexemer, A.; Amassian, A. *Adv. Mater.* **2013**, *25*, 1923−1929.
(11) Ihn, K. J.; Moulton, J.; Smith, P. *J. Polym. Sci., Part B: Polym. Phys.* **1993**, *31*, 735−742.
(12) Joseph Kline, R.; McGehee, M. D.; Toney, M. F. *Nat. Mater.* **2006**, *5*, 222−228.
(13) Berson, S.; De Bettignies, R.; Bailly, S.; Guillerez, S. *Adv. Funct. Mater.* **2007**, *17*, 1377−1384.
(14) Moule, A. J.; Meerholz, K. *Adv. Funct. Mater.* **2009**, *19*, 3028−3036.
(15) van Bavel, S. S.; Sourty, E.; de With, G.; Loos, J. *Nano Lett.* **2009**, *9*, 507−513.
(16) Krebs, F. C.; Espinosa, N.; Hösel, M.; Søndergaard, R. R.; Jørgensen, M. *Adv. Mater.* **2013**, *26*, 29−39.
(17) Wu, Z. Y.; Petzold, A.; Henze, T.; Thurn-Albrecht, T.; Lohwasser, R. H.; Sommer, M.; Thelakkat, M. *Macromolecules* **2010**, *43*, 4646−4653.
(18) Taylor, K. A.; Glaeser, R. M. *Science* **1974**, *186*, 1036−1037.
(19) Frederik, P. M.; Stuart, M. C. A.; Schrijvers, A.; Bomans, P. H. H. *Scanning Microsc.* **1989**, *3*, 277−284.
(20) Friedrich, H.; Frederik, P. M.; de With, G.; Sommerdijk, N. A. J. M. *Angew. Chem., Int. Ed.* **2010**, *49*, 7850−7858.
(21) van Herrikhuyzen, J.; George, S. J.; Vos, M. R. J.; Sommerdijk, N. A. J. M.; Ajayaghosh, A.; Meskers, S. C. J.; Schenning, A. P. H. J. *Angew. Chem., Int. Ed.* **2007**, *46*, 1825−1828.
(22) Balmes, O.; Malm, J.-O.; Karlsson, G.; Bovin, J.-O. *J. Nanopart. Res.* **2005**, *6*, 569−576.
(23) Oostergetel, G. T.; Esselink, F. J.; Hadziioannou, G. *Langmuir* **1995**, *11*, 3721−3724.
(24) Cui, H.; Hodgdon, T. K.; Kaler, E. W.; Abezgauz, L.; Danino, D.; Lubovsky, M.; Talmon, Y.; Pochan, D. J. *Soft Matter* **2007**, *3*, 945−955.
(25) Tashiro, K.; Minagawa, Y.; Kobayashi, M.; Morita, S.; Kawai, T.; Yoshino, K. *Synth. Met.* **1993**, *55*, 321−328.
(26) Winokur, M. J.; Spiegel, D.; Kim, Y.; Hotta, S.; Heeger, A. J. *Synth. Met.* **1989**, *28*, C419−C426.
(27) Sandstedt, C. A.; Rieke, R. D.; Eckhardt, C. J. *Chem. Mater.* **1995**, *7*, 1057−1059.
(28) Yamagata, H.; Spano, F. C. *J. Chem. Phys.* **2012**, *136*, 184901.
(29) Roehling, J. D.; Arslan, I.; Moulé, A. J. *J. Mater. Chem.* **2012**, *22*, 2498.
(30) Kanemoto, K.; Sudo, T.; Akai, I.; Hashimoto, H.; Karasawa, T.; Aso, Y.; Otsubo, T. *Phys. Rev. B* **2006**, *73*, 235203.
(31) Drummy, L. F.; Davis, R. J.; Moore, D. L.; Durstock, M.; Vaia, R. A.; Hsu, J. W. P. *Chem. Mater.* **2011**, *23*, 907−912.
(32) Dudenko, D.; Kiersnowski, A.; Shu, J.; Pisula, W.; Sebastiani, D.; Spiess, H. W.; Hansen, M. R. *Angew. Chem., Int. Ed.* **2012**, *51*, 11068−11072.
(33) Kayunkid, N.; Uttiya, S.; Brinkmann, M. *Macromolecules* **2010**, *43*, 4961−4967.
(34) Tashiro, K.; Ono, K.; Minagawa, Y.; Kobayashi, M.; Kawai, T.; Yoshino, K. *J. Polym. Sci., Part B: Polym. Phys.* **1991**, *29*, 1223−1233.
(35) Kim, Y.; Cook, S.; Tuladhar, S. M.; Choulis, S. A.; Nelson, J.; Durrant, J. R.; Bradley, D. D. C.; Giles, M.; McCulloch, I.; Ha, C.-S.; Ree, M. *Nat. Mater.* **2006**, *5*, 197−203.
(36) Hartmann, L.; Tremel, K.; Uttiya, S.; Crossland, E.; Ludwigs, S.; Kayunkid, N.; Vergnat, C.; Brinkmann, M. *Adv. Funct. Mater.* **2011**, *21*, 4047−4057.
(37) Mena-Osteritz, E.; Meyer, A.; Langeveld-Voss, B. M. W.; Janssen, R. A. J.; Meijer, E. W.; Bauerle, P. *Angew. Chem., Int. Ed.* **2000**, *39*, 2680−2684.
(38) Pouget, E. M.; Bomans, P. H. H.; Goos, J. A. C. M.; Frederik, P. M.; de With, G.; Sommerdijk, N. A. J. M. *Science* **2009**, *323*, 1455−1458.
(39) Dey, A.; de With, G.; Sommerdijk, N. A. J. M. *Chem. Soc. Rev.* **2010**, *39*, 397−409.